


## Unconventional surface responses of fourfold-degenerate Dirac-nodal-line semimetals in sonic crystals

Chang-Yin Ji<sup>1,2,‡</sup>, Jijie Tang<sup>1,‡</sup>, Xiao-Ping Li<sup>3,‡</sup>, Zheng Tang<sup>1</sup>, Di Zhou<sup>1</sup>, Yeliang Wang<sup>2</sup>,  
Feng Li<sup>1,\*</sup>, Jiafang Li<sup>1,†</sup> and Yugui Yao<sup>1</sup>

<sup>1</sup>Key Laboratory of Advanced Optoelectronic Quantum Architecture and Measurement (MOE), Beijing Key Laboratory of Nanophotonics and Ultrafine Optoelectronic Systems, and School of Physics, Beijing Institute of Technology, Beijing 100081, China

<sup>2</sup>School of Integrated Circuits and Electronics, Ministry of Industry and Information Technology (MIIT) Key Laboratory for Low-Dimensional Quantum Structure and Devices, Beijing Institute of Technology, Beijing 100081, China

<sup>3</sup>School of Physical Science and Technology, Inner Mongolia University, Hohhot 010021, China

 (Received 5 July 2023; revised 6 November 2023; accepted 29 November 2023; published 28 December 2023)

Three-dimensional nodal-line semimetals (NLSMs) are of remarkable importance for both enriching topological physics and wave management. However, NLSMs realized in acoustic systems are twofold band degenerate and are called Weyl NLSMs. Here, we report on the experimental observation of Dirac NLSMs with fourfold degeneracy in sonic crystals. We reveal that the topological properties of the Dirac NLSMs are entirely *different* than those of the conventional Weyl NLSMs. The Berry phase related to the Dirac nodal line (DNL) is  $2\pi$ , which results in surface responses of the Dirac NLSMs in two radically different situations: a torus surface state occupying the entire surface Brillouin zone (SBZ) and one without any surface state in the SBZ. We further reveal that topological surface arcs caused by the DNL can change from open to closed contours. The findings of Dirac NLSMs and their unique surface response may bring about exciting frontiers for the flexible manipulation of acoustic surface waves.

DOI: [10.1103/PhysRevApplied.20.064047](https://doi.org/10.1103/PhysRevApplied.20.064047)

### I. INTRODUCTION

Three-dimensional (3D) topological semimetals (TSMs) have been one of the most flourishing research fields since the discovery of the Weyl fermion in solid materials [1]. Compared with topological insulators, 3D TSMs open another new research perspective in which to explore the plentiful exotic topological phenomena and electronic transport [2–4], including topologically protected surface states, the chiral anomaly [5], the planar Hall effect [6,7], the intrinsic anomalous Hall effect [8,9], quantized circulation of the anomalous shift [10], and so on. According to the dimension of the band degeneracies of 3D TSMs [11], we can classify them into zero-dimensional (0D) nodal points, one-dimensional (1D) nodal lines (NLs) [12–22], and two-dimensional (2D) nodal-surface semimetals [23,24]. Since the topological band theory in condensed-matter physics is fundamental and universal to classical wave systems, the concepts of TSMs have recently been extended from quantum systems into photonic and acoustic systems. Experimental observations have shown

that the unprecedented flexibility in design afforded by macroscopic meta-atoms has led to the discovery of Weyl semimetals and Dirac semimetals analogous to classical waves [19,25–30]. The experimental results provide solid evidence for Weyl- and Dirac-point-endowed topological properties, such as the Fermi arcs arising from the Weyl point [25–27], the gapless helicoid surface states arising from the Dirac point [28,29], and the high-order hinge states connecting the projected Dirac or Weyl points [31–33].

Compared to the widely studied nodal-point semimetals in classical systems, the 1D nodal lines (NLs) are still poorly studied [11,12,34]. The configurations and topological properties of nodal lines are more diverse compared to nodal-point semimetals. According to the shape of the 1D NLs and the connectivities between NLs, they can be classified into different types, such as the nodal curve, nodal ring, nodal chain, nodal link, nodal knot, and so on [11]. According to the number of band degeneracies, NLs can be divided into Weyl NLs with twofold line degeneracy and Dirac NLs with fourfold line degeneracy [35,36]. The Berry phase of the Weyl NLs is  $\pi$ , as shown in Figs. 1(a) and 1(b). This results in the drumhead surface states (SSs), which can only cover a small region of the BZ, e.g., the region outside or inside the nodal ring, as

\*phlifeng@bit.edu.cn

†jiafangli@bit.edu.cn

‡These authors contribute equally to this work.

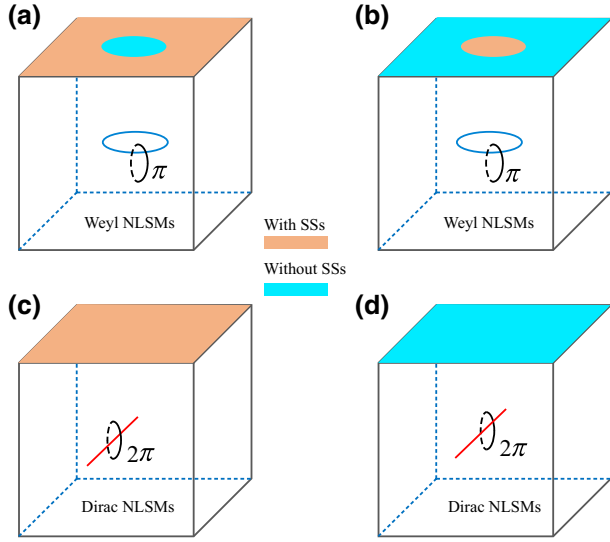


FIG. 1. A schematic illustration of the Berry phase and the related surface states (SSs) of the nodal-line semimetals (NLSMs). (a),(b) Weyl NLSMs with twofold degeneracy along the line in momentum space. The Berry phase of the Weyl NLSMs is  $\pi$ , which leads to drumhead SSs that occupy the region outside the nodal ring in (a) or inside the nodal ring in (b). (c),(d) Dirac NLSMs with fourfold degeneracy along the line in momentum space. The Berry phase of the Dirac NLSMs is  $2\pi$ . The Dirac NLSMs have two distinct surface responses: a torus SS occupying the entire surface Brillouin zone (SBZ) in (c) or without any SSs in (d).

shown in Figs. 1(a) and 1(b). In current acoustic systems, only WNL semimetals (NLSMs) have been realized, while DNL semimetals are still lacking.

Here, we theoretically propose and experimentally realize Dirac NLSMs to fill this void. Going one step further, we demonstrate that the topological properties and surface responses caused by the Dirac nodal line (DNL) are distinct from those of the Weyl nodal line (WNL). The Berry phase of the DNL is  $2\pi$ , as shown in Figs. 1(c) and 1(d). Such a  $2\pi$  Berry phase leads to intriguing surface responses that are entirely different from that of the WNL. As shown in Fig. 1(c), the SSs can occupy the entire SBZ, forming the torus SSs. The other scenario is that the whole BZ has no SSs, as shown in Fig. 1(d). Compared to the situation of the surface responses induced by Weyl NLSMs, the Dirac NLSMs have unconventional surface responses.

## II. THEORETICAL DESIGN

The designed acoustic Dirac NLSM is shown in Fig. 2(a): it is an orthorhombic structure and it belongs to space group  $Pnma$  (No. 62). The lattice periods along the  $x$ ,  $y$ , and  $z$  directions are  $p_x = 1.84$  cm,  $p_y = 1.6$  cm, and  $p_z = 1.52$  cm, respectively. There are four symmetry operators for the Dirac NLSMs in Fig. 2(a), two screw rotations,  $\tilde{C}_{2z} : (x, y, z) \rightarrow (-x + p_x/2, -y, z + p_z/2)$  and

$\tilde{C}_{2y} : (x, y, z) \rightarrow (-x, y + p_y/2, -z)$ , spatial inversion  $\mathcal{P} : (x, y, z) \rightarrow (-x, -y, -z)$ , and time-reversal symmetry  $\mathcal{T}$ . The bulk and surface BZs are shown in Fig. 2(b). Figure 2(c) shows the band structure of the designed acoustic crystal illustrated in Fig. 2(a). It can be seen that there exists fourfold line degeneracy along the high-symmetry line  $SR$ , which confirms that the DNL is present. The frequency range of the DNL is from 13.07 kHz to 13.14 kHz. The DNL is an open straight nodal line and is located in a fairly wide and clean frequency range, which can serve as an ideal DNL.

We further use symmetry analysis to illustrate why the DNL appears at the hinge between the  $k_x = \pi/p_x$  and  $k_y = \pi/p_y$  planes. For an arbitrary  $D$  point located on the line  $SR$ , its symmetry operators can be expressed as  $\tilde{C}_{2z}$ ,  $\tilde{M}_y : (x, y, z) \rightarrow (x, -y + p_y/2, z)$ , and a combined operator  $\mathcal{A} = \tilde{C}_{2y}\mathcal{T}$ . They meet in the following form:

$$\tilde{C}_{2z}^2 = 1, \quad \tilde{M}_y^2 = 1, \quad \mathcal{A}^2 = -1. \quad (1)$$

The combination of  $\tilde{M}_y$  and  $\tilde{C}_{2z}$  yields

$$\begin{aligned} \tilde{M}_y\tilde{C}_{2z} : (x, y, z) &\rightarrow (-x + p_x/2, y + p_y/2, z + p_z/2), \\ \tilde{C}_{2z}\tilde{M}_y : (x, y, z) &\rightarrow (-x + p_x/2, y - p_y/2, z + p_z/2). \end{aligned} \quad (2)$$

Let  $|\varphi\rangle$  be an eigenstate of  $\tilde{C}_{2z}$  at the  $D$  point. One can obtain  $\tilde{M}_y\tilde{C}_{2z}|\varphi\rangle = e^{ik_y p_y/2} [e^{i(k_x p_x/2 + k_z p_z/2)} M_x |\varphi\rangle]$  and  $\tilde{C}_{2z}\tilde{M}_y|\varphi\rangle = e^{-ik_y p_y/2} [e^{i(k_x p_x/2 + k_z p_z/2)} M_x |\varphi\rangle]$ . Due to  $k_y = \pi/p_y$  at the  $D$  point, one can obtain  $\tilde{M}_y\tilde{C}_{2z} = -\tilde{C}_{2z}\tilde{M}_y$ . A similar analysis can be applied to the combination operators of  $\tilde{C}_{2z}\mathcal{A}$  and  $\tilde{M}_y\mathcal{A}$ : one can obtain  $\tilde{C}_{2z}\mathcal{A} = \mathcal{A}\tilde{C}_{2z}$  and  $\tilde{M}_y\mathcal{A} = -\mathcal{A}\tilde{M}_y$ . For convenience of discussion, we take  $|\varphi\rangle$  as the eigenstate of the eigenvalue of 1 of  $\tilde{C}_{2z}$ . Then, we can have

$$\tilde{C}_{2z}\tilde{M}_y|\varphi\rangle = -\tilde{M}_y|\varphi\rangle, \quad \langle\varphi|\tilde{M}_y|\varphi\rangle = 0. \quad (3)$$

Thus, the eigenstates of  $|\varphi\rangle$  and  $\tilde{M}_y|\varphi\rangle$  are a pair of degenerate states. Since there exists an antiunitary operator  $\mathcal{A}$  on the high-symmetry line  $SR$ ,  $|\varphi\rangle$  and  $\tilde{M}_y|\varphi\rangle$  have Kramers-like counterparts of  $\mathcal{A}|\varphi\rangle$  and  $\mathcal{A}\tilde{M}_y|\varphi\rangle$ , respectively. In addition, since  $\tilde{C}_{2z}$  and  $\mathcal{A}$  are commutative, the states and their Kramers-like counterparts are linearly independent. Thus, there must exist four degenerate states of  $|\varphi\rangle$ ,  $\tilde{M}_y|\varphi\rangle$ ,  $\mathcal{A}|\varphi\rangle$ , and  $\mathcal{A}\tilde{M}_y|\varphi\rangle$  at any  $\mathbf{k}$  point on the high-symmetry line  $SR$ . Figure 2(d) shows the band dispersion around a certain  $\mathbf{k}$  point along  $SR$ . It can be seen that the Dirac point splits at an ordinary  $\mathbf{k}$  point, forming a Dirac-shaped dispersion.

Using the  $\mathbf{k} \cdot \mathbf{p}$  perturbation method, we also derive a four-band Hamiltonian to gain a deeper insight into the

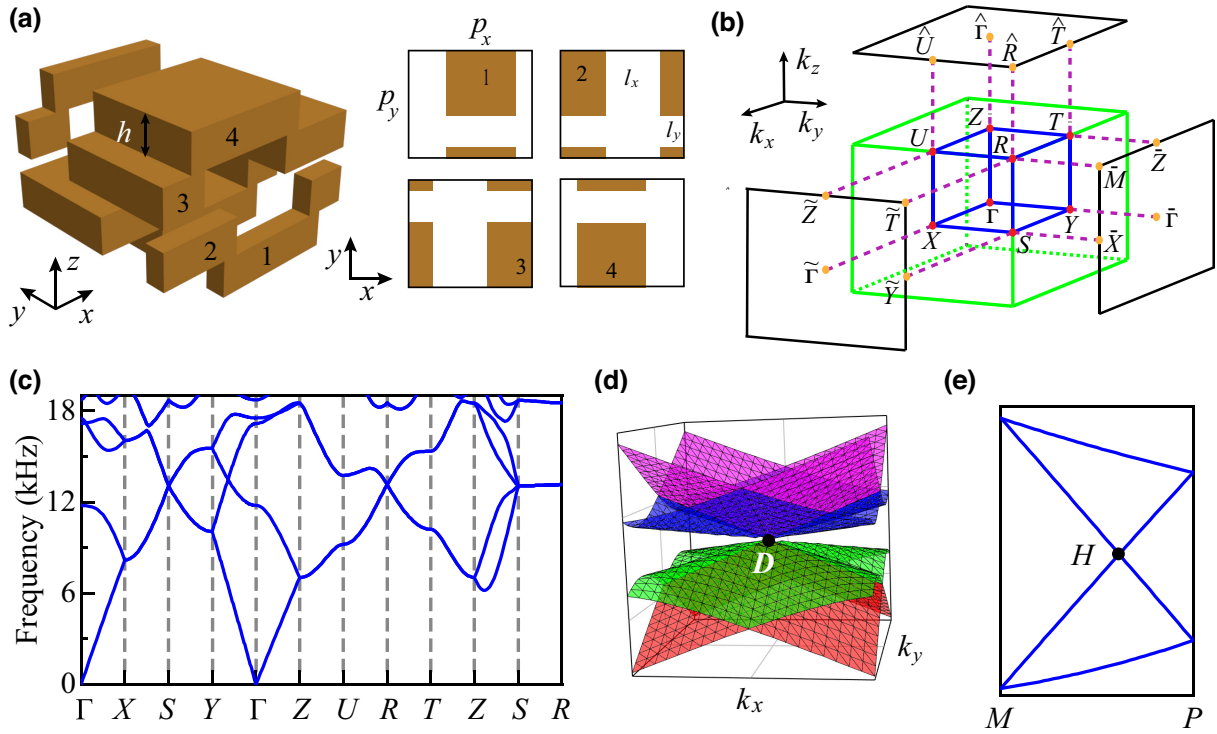


FIG. 2. (a) The unit-cell structure of the designed layer acoustic Dirac NLSMs. The lattice periods along the  $x$ ,  $y$ , and  $z$  directions are  $p_x = 1.84$  cm,  $p_y = 1.6$  cm, and  $p_z = 1.52$  cm, respectively. The cell contains four layers, where the first and second layers are connected to each other and the third and fourth layers are connected to each other. The center positions of the first to fourth layers along the  $z$  direction are  $z_0, p_z/2 - z_0, p_z/2 + z_0$ , and  $p_z - z_0$ , respectively.  $z_0 = 0.23$  cm. The thickness of each layer is  $h = 0.3$  cm. The widths of the air slits in each layer along the  $x$  and  $y$  directions are  $l_x = 0.8$  cm and  $l_y = 0.46$  cm, respectively. (b) The bulk Brillouin zone (BZ) and the (100), (010), and (001) surface BZs. (c) The bulk band structure of the Dirac-Weyl NLSMs in (a). (d) A Dirac-shaped dispersion around a generic  $\mathbf{k}$  point along  $SR$ . (e) An hourglass-shaped dispersion along a generic path of  $MP$ , where  $M$  and  $P$  are arbitrary points on the paths  $XS$  and  $SY$ , respectively.

physics around the DNL:

$$\mathcal{H}_{DNL} = a_0 + a_1 k_z + \begin{pmatrix} h_0 & h_1 \\ h_1^\dagger & h_0 \end{pmatrix}, \quad (4)$$

where  $h_0 = v_x \delta k_x \sigma_x + v_y \delta k_y \sigma_y$  and  $h_1 = b_1 \delta k_x \sigma_y + b_2 \delta k_y \sigma_x$ . Here,  $a_i$  and  $b_i$  are the real and complex numbers, respectively.  $(\delta k_x, \delta k_y)$  denotes the momentum deviation from  $(\pi/p_x, \pi/p_y)$ .  $\sigma_i$  is the Pauli matrix.  $h_0$  describes the Dirac points in the  $k_x$ - $k_y$  plane, the Berry phase of which is  $\pi$ .  $v_x$  and  $v_y$  are the Dirac velocities along the  $x$  and  $y$  directions, respectively. Figure 2(d) shows the dispersion around the Dirac point. More interestingly, the Hamiltonian of Eq. (4) shows that the Berry phase of the DNL is  $2\pi$ , which is very different from that of the WNL.

Due to the nonsymmorphic symmetry of the structure, it should be noted that our designed acoustic crystal also has an unrealized hourglass WNL in the acoustic system. The frequency of the WNL is approximately 13.40 kHz. Figure 2(e) shows the hourglass-shaped dispersion along the patch of  $MP$ . The cross point  $H$  must form a ring in the  $k_x$ - $k_y$  plane, which is guaranteed by the symmetry

operators of  $\tilde{M}_z = \tilde{C}_{2z} \mathcal{P}$  and  $\mathcal{P}T$ . The Berry phase of the hourglass WNL is the same as that of an ordinary nodal line, which is also  $\pi$ . Thus, our designed acoustic crystal provides an excellent platform to study the differences between the WNL and the DNL.

An important feature of NLSMs is the appearance of topologically protected SSs on their surfaces. To better reveal the surface response of the NLSMs, we first give the Zak-phase distribution for the (100), (010), and (001) planes. The Zak phase is the Berry phase of a straight line perpendicular to the surface and passing through the bulk BZ. The existence of  $\mathcal{P}$  requires the Zak phase to be quantized, the values being 0 or  $\pi$ . The calculated Zak-phase distributions are shown in Figs. 3(a)–3(c). It should be noted that the (100) and (010) planes are parallel to the DNL, while the (001) plane is parallel to the WNL. Figures 3(a) and 3(b) show that the Zak phase is equal to 0 and  $\pi$  in the whole BZ of the (100) and (010) planes, respectively. This is caused by the  $2\pi$  Berry phase of the DNL. For the (100) and (010) planes, the Zak phase of a straight line perpendicular to the surface cannot be changed until the line passes through the DNL. As it passes through the DNL, its

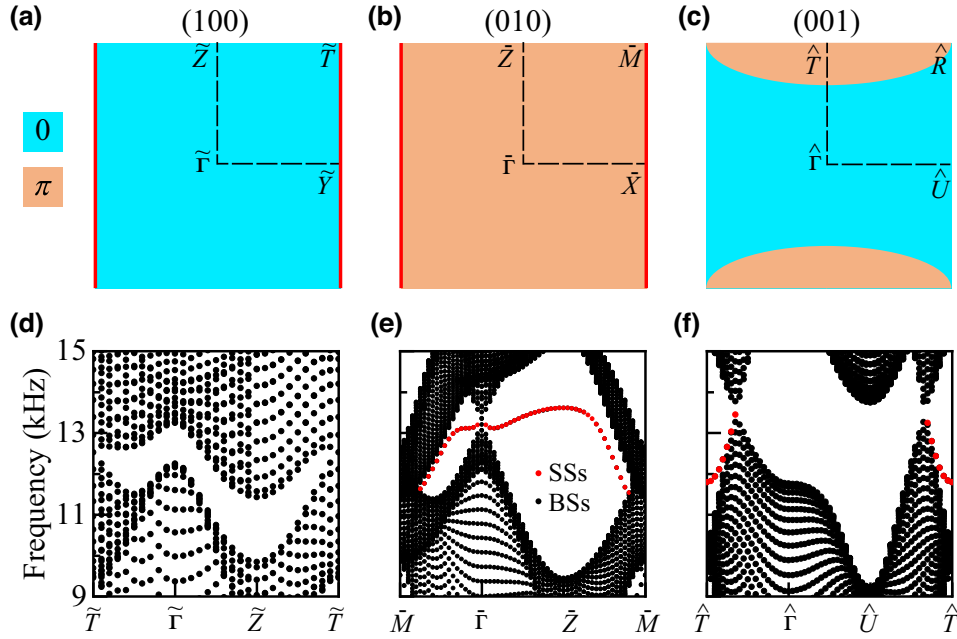


FIG. 3. (a)–(c) The Zak-phase distributions on the surfaces of (100), (010), and (001), respectively. The cyan and orange regions indicate the Zak phases 0 and  $\pi$ , respectively. The red lines in (a) and (b) show the position of the DNL. (d)–(f) Simulated surface spectra on the (100), (010), and (001) surfaces, respectively. The red and black dots represent the nontrivial surface states (SSs) and bulk states (BSs), respectively.

Zak phase changes to  $2\pi$ . Since the Zak phase is defined mod  $2\pi$ , the Zak phase of the entire BZ is the same, either 0 as in Fig. 3(a) or  $\pi$  as in Fig. 3(b). The result in Fig. 3(c) shows that only a small region of the Zak phase is  $\pi$ , which results from the  $\pi$  Zak phase of the hourglass WNL. Similarly, the Zak phase of the straight line perpendicular to (001) plane will change to  $\pi$  once it passes through the hourglass WNL. This necessarily results in a Zak phase of 0 in one region and a Zak phase of  $\pi$  in the complementary region. The simulated surface spectra are shown in Figs. 3(d)–3(f). It can be seen that there are no SSs in the whole BZ of (100) plane due to the Zak phase being 0, as shown in Fig. 3(d). However, the result in Fig. 3(e) shows that the SSs cover the whole BZ, which is consistent with the Zak-phase distribution of  $\pi$ . Since the 2D BZ can be regarded as a torus, such a surface state is called a torus surface state. The SSs in Fig. 3(f) is the same as the usual Weyl NLSMs, featuring drumheadlike SSs. Thus, our NLSMs can have three types of surface responses at the same time, namely, no surface state, torus surface states, and drumheadlike surface states. This rich surface response makes the Dirac NLSMs remarkably different from that of the widely studied Weyl NLSMs.

### III. EXPERIMENTAL OBSERVATIONS

We further conduct an acoustic experiment to investigate the fascinating topological properties of the Dirac

NLSMs. The sample is manufactured with 3D printing, as shown in Fig. 4(a). The sample contains  $19 \times 19 \times 19$  unit cells with a size of  $34.96 \times 30.4 \times 28.88$  mm. To measure the bulk band structure, a tiny microphone is inserted into the sample as a sound source to excite the Bloch states. The frequency range of the source is 1–19 kHz. Then, we use a moving detector to record the spatial distributions of both the phase and amplitude of the Bloch states. Finally, the bulk band structure in the momentum space can be obtained by Fourier transforming the measured Bloch states in real space. The measured bulk band structure along the high-symmetry line of the BZ is shown in Fig. 4(b), which is consistent with the theoretical calculation result [see the magenta solid lines in Fig. 4(b)]. The experimental results clearly show that there exists a straight DNL in the path of the line  $SR$ . The experimentally measured frequency range of the DNL appears to be wide due to the limited sample size. The experimental results also observe the cross point generated by the hourglass WNL along the path of  $\Gamma Y$ .

Next, we experimentally investigate the surface responses of the (010) and (001) surfaces of the Dirac NLSMs. The resin plate are fabricated on the (010) and (001) surfaces to mimic the hard-wall surface boundary used in full-wave simulations. This is due to the fact that open boundary conditions result in no topological surface states (see the results in Fig. S4 of the Supplemental Material [37]). The method of surface pump-probe spectroscopy

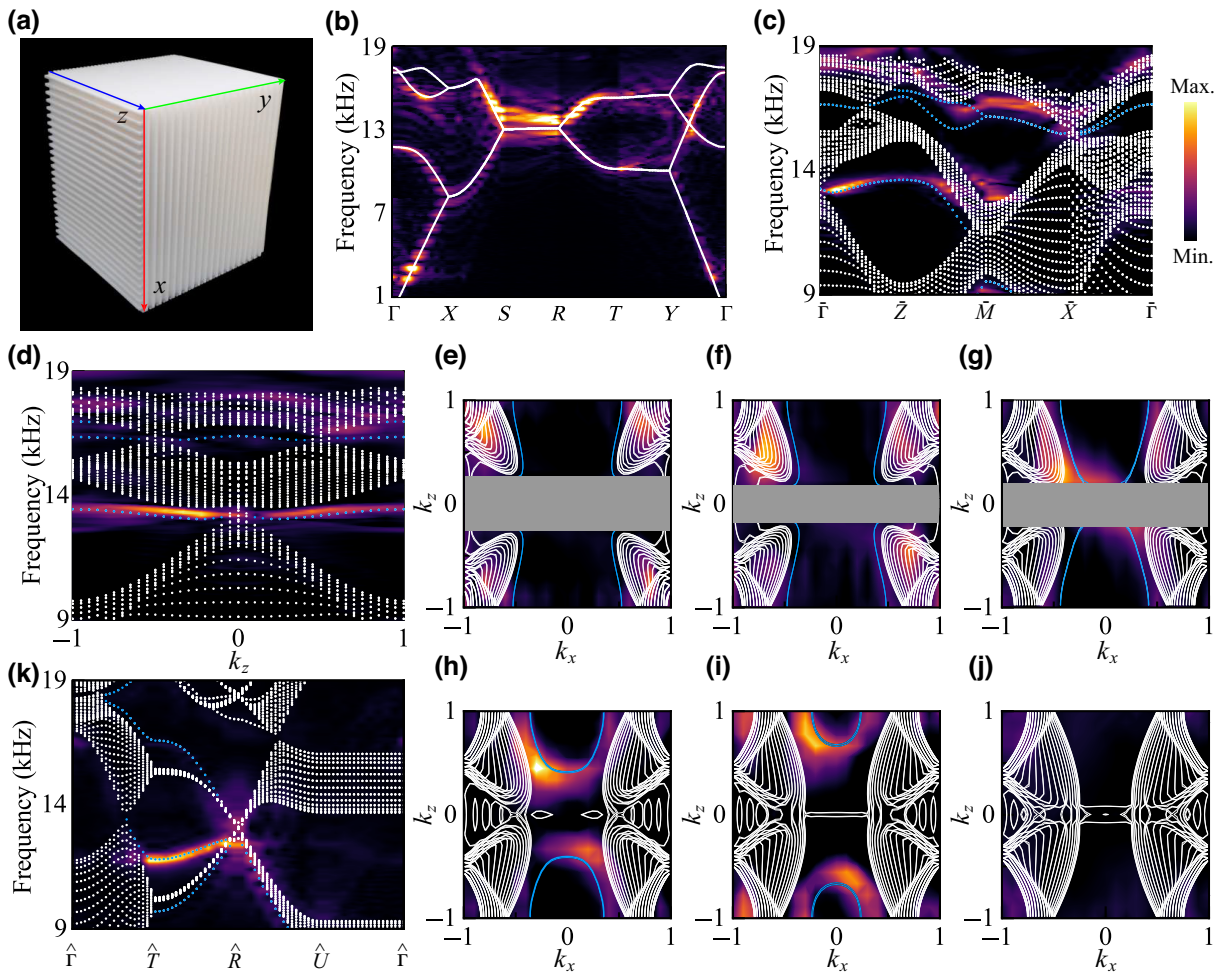


FIG. 4. (a) A photograph of the experimental sample fabricated by 3D printing. (b) The experimentally measured (colors) bulk band structure along the high-symmetry lines of the bulk BZ in Fig. 1(b). The magenta solid lines are the simulated bulk band structure. (c) The experimentally measured surface dispersions of the (010) plane. (d) Measured dispersions with  $k_x = 0.3\pi/p_x$  for the (010) plane. (e)–(i) The measured isofrequency contours (colored) of the (010) plane for various frequencies: (e)  $f = 12.7$  kHz; (f)  $f = 12.9$  kHz; (g)  $f = 13.1$  kHz; (h)  $f = 13.3$  kHz; (i)  $f = 13.5$  kHz; (j)  $f = 13.7$  kHz. The red curves show the topological surface arcs. (k) The experimentally measured surface dispersions of the (001) plane. The dot plot is the result of theoretical calculations. The red and black dots represent surface states and bulk states, respectively.

is used to obtain the surface dispersions. A subwavelength acoustic source is placed at the corresponding surface and then the detector scans the Bloch states near the sample surface. The measured surface dispersions of the (010) surface are shown in Fig. 4(c) and are in good agreement with the simulation results (see the red dots). The incomplete match between the experimental results and the theory is mainly caused by sample-preparation errors and measurement uncertainties. To show that the surface states on the (010) surface cover the entire BZ, we also present the results for  $k_x = 0.3\pi/p_x$ , as shown in Fig. 4(d). The presence of surface states clearly confirms this [see Fig. 4(d)]. The isofrequency contours of the (010) surface for different frequencies are shown in Figs. 4(e)–4(j). Although the Zak phase of the 010 surface is  $\pi$ , the surface arcs do not exist throughout the  $k_x$  and  $k_z$  space due to the dispersion of

surface states, similarly to the saddle and influence of bulk states (see the results in Fig. S1 of the Supplemental Material [37]). When the measurement frequency is lower than the DNL frequency range, the starting point of the topological surface arc starts from the boundary of the BZ and ends at the bulk state [see the red curves in Figs. 4(e)–4(g)—the gray regions in Figs. 4(e)–4(g) are the bulk-band projections]. The topological surface arc is an open profile and its starting and ending positions will change with the measurement frequency, shown in Figs. 4(e)–4(g). However, the topological surface arc is a closed profile when the measurement frequency is larger than the DNL frequency range, as shown in Figs. 4(h)–4(i). When the measurement frequency exceeds a critical value, the topological surface states disappear [see Fig. 4(j)]. The transition from an open contour to a closed contour after the DNL is due

to the frequency of the DNL being near the saddle point of the saddle band dispersion (see the results in Fig. S1 of the Supplemental Material [37]). Therefore, the surface response of the DNL differs from that of Weyl semimetals, where the Fermi arcs are always open profiles. The measured surface dispersions of the (001) surface are shown in Fig. 4(k), which clearly shows that the topological state occupies only part of the BZ. It should be noted that the topological surface state is not robust to defects when the system has time-reversal symmetry (see the experimental results in Fig. S3 of the Supplemental Material [37]). Because the surface states near high frequencies (17 kHz) and low frequencies (9 kHz) deviate from the frequency range of the DNL and the WNL, they are not caused by the topological properties of the NL and are trivial surface states produced by hard-boundary truncation (see Figs. 2 and 4).

#### IV. CONCLUSIONS

In summary, we theoretically and experimentally realize the long-sought-after DNL semimetals. We further demonstrate that the Berry phase of DNLs is  $2\pi$ , which is completely different from that of WNLs, with a  $\pi$  Berry phase. This also leads to a completely different surface response for parallel DNLs than conventional Weyl NLSMs. For the designed acoustic crystal, the (100) plane has no surface states, while the surface states can cover the whole BZ for the (010) plane and thereby the torus surface states are realized. Meanwhile, this system also has drumheadlike surface states caused by the hourglass WNL. Further, we reveal that the topological surface arcs change from open to closed contours on the (010) plane, which is very different from those of Weyl semimetals. The versatile surface response of the Dirac NLSMs provides an ideal platform for manipulating sound waves, e.g., through the use of a surface acoustic wave isolator and an omnidirectional surface acoustic wave device.

#### ACKNOWLEDGMENTS

This work is supported by the National Natural Science Foundation of China (Grants No. 12204041, No. 11734003, No. 61975016, No. 12061131002, No. 12102039, No. 12272040, and No. 92163206); the Strategic Priority Research Program of the Chinese Academy of Sciences (Grant No. XDB30000000); the National Key R&D Program of China (Grants No. 2020YFA0308800 and No. 2021YFA1400100); the National Science Foundation of Beijing Municipality (Grants No. Z190006 and No. 1212013); and the China Postdoctoral Science Foundation (Grant No. 2021M700436).

*Note added.*—Recently we have become aware of an independent discovery of the Dirac NLSM and its torus surface states [38].

- [1] X. Wan, A. M. Turner, A. Vishwanath, and S. Y. Savrasov, Topological semimetal and Fermi-arc surface states in the electronic structure of pyrochlore iridates, *Phys. Rev. B* **83**, 205101 (2011).
- [2] N. Armitage, E. Mele, and A. Vishwanath, Weyl and Dirac semimetals in three-dimensional solids, *Rev. Mod. Phys.* **90**, 015001 (2018).
- [3] J. Hu, S.-Y. Xu, N. Ni, and Z. Mao, Transport of topological semimetals, *Annu. Rev. Mater. Res.* **49**, 207 (2019).
- [4] B. Lv, T. Qian, and H. Ding, Experimental perspective on three-dimensional topological semimetals, *Rev. Mod. Phys.* **93**, 025002 (2021).
- [5] A. Zyuzin and A. Burkov, Topological response in Weyl semimetals and the chiral anomaly, *Phys. Rev. B* **86**, 115133 (2012).
- [6] N. Kumar, S. N. Guin, C. Felser, and C. Shekhar, Planar Hall effect in the Weyl semimetal GdPtBi, *Phys. Rev. B* **98**, 041103 (2018).
- [7] D. Ma, H. Jiang, H. Liu, and X. Xie, Planar Hall effect in tilted Weyl semimetals, *Phys. Rev. B* **99**, 115121 (2019).
- [8] A. A. Zyuzin and R. P. Tiwari, Intrinsic anomalous Hall effect in type-II Weyl semimetals, *JETP Lett.* **103**, 717 (2016).
- [9] G. S. Thakur, P. Vir, S. N. Guin, C. Shekhar, R. Wehrich, Y. Sun, N. Kumar, and C. Felser, Intrinsic anomalous Hall effect in Ni-substituted magnetic Weyl semimetal  $\text{Co}_3\text{Sn}_2\text{S}_2$ , *Chem. Mater.* **32**, 1612 (2020).
- [10] Y. Liu, Z.-M. Yu, C. Xiao, and S. A. Yang, Quantized circulation of anomalous shift in interface reflection, *Phys. Rev. Lett.* **125**, 076801 (2020).
- [11] H. Park, W. Gao, X. Zhang, and S. S. Oh, Nodal lines in momentum space: Topological invariants and recent realizations in photonic and other systems, *Nanophotonics* **11**, 2779 (2022).
- [12] H. Qiu, C. Qiu, R. Yu, M. Xiao, H. He, L. Ye, M. Ke, and Z. Liu, Straight nodal lines and waterslide surface states observed in acoustic metacrystals, *Phys. Rev. B* **100**, 041303 (2019).
- [13] J. Lu, X. Huang, M. Yan, F. Li, W. Deng, and Z. Liu, Nodal-chain semimetal states and topological focusing in phononic crystals, *Phys. Rev. Appl.* **13**, 054080 (2020).
- [14] M. Xiao, X.-Q. Sun, and S. Fan, Nodal chain semimetal in geometrically frustrated systems, *Phys. Rev. B* **99**, 094206 (2019).
- [15] Z.-G. Geng, Y.-G. Peng, Y.-X. Shen, Z. Ma, R. Yu, J.-H. Gao, and X.-F. Zhu, Topological nodal line states in three-dimensional ball-and-stick sonic crystals, *Phys. Rev. B* **100**, 224105 (2019).
- [16] Z. Wang, Z. Wang, H. Li, J. Luo, X. Wang, Z. Liu, and H. Yang, Weyl points and nodal lines in acoustic synthetic parameter space, *Appl. Phys. Express* **14**, 077002 (2021).
- [17] H. Xue, Y. Yang, and B. Zhang, Topological acoustics, *Nat. Rev. Mater.* **7**, 974 (2022).
- [18] W. Gao, B. Yang, B. Tremain, H. Liu, Q. Guo, L. Xia, A. P. Hibbins, and S. Zhang, Experimental observation of photonic nodal line degeneracies in metacrystals, *Nat. Commun.* **9**, 950 (2018).
- [19] L. Xia, Q. Guo, B. Yang, J. Han, C.-X. Liu, W. Zhang, and S. Zhang, Observation of hourglass nodal lines in photonics, *Phys. Rev. Lett.* **122**, 103903 (2019).

- [20] S. Hu, Z. Guo, H. Jiang, and H. Chen, Photonic Dirac nodal-line semimetals realized by a hypercrystal, *Phys. Rev. Res.* **4**, 023047 (2022).
- [21] T. Kawakami and X. Hu, Symmetry-guaranteed nodal-line semimetals in an fcc lattice, *Phys. Rev. B* **96**, 235307 (2017).
- [22] B. Song, C. He, S. Niu, L. Zhang, Z. Ren, X.-J. Liu, and G.-B. Jo, Observation of nodal-line semimetal with ultracold fermions in an optical lattice, *Nat. Phys.* **15**, 911 (2019).
- [23] Y. Yang, J.-P. Xia, H.-X. Sun, Y. Ge, D. Jia, S.-Q. Yuan, S. A. Yang, Y. Chong, and B. Zhang, Observation of a topological nodal surface and its surface-state arcs in an artificial acoustic crystal, *Nat. Commun.* **10**, 5185 (2019).
- [24] M. Xiao, L. Ye, C. Qiu, H. He, Z. Liu, and S. Fan, Experimental demonstration of acoustic semimetal with topologically charged nodal surface, *Sci. Adv.* **6**, eaav2360 (2020).
- [25] H. He, C. Qiu, L. Ye, X. Cai, X. Fan, M. Ke, F. Zhang, and Z. Liu, Topological negative refraction of surface acoustic waves in a Weyl phononic crystal, *Nature* **560**, 61 (2018).
- [26] F. Li, X. Huang, J. Lu, J. Ma, and Z. Liu, Weyl points and Fermi arcs in a chiral phononic crystal, *Nat. Phys.* **14**, 30 (2018).
- [27] H. He, C. Qiu, X. Cai, M. Xiao, M. Ke, F. Zhang, and Z. Liu, Observation of quadratic Weyl points and double-helicoid arcs, *Nat. Commun.* **11**, 1820 (2020).
- [28] H. Cheng, Y. Sha, R. Liu, C. Fang, and L. Lu, Discovering topological surface states of Dirac points, *Phys. Rev. Lett.* **124**, 104301 (2020).
- [29] X. Cai, L. Ye, C. Qiu, M. Xiao, R. Yu, M. Ke, and Z. Liu, Symmetry-enforced three-dimensional Dirac phononic crystals, *Light Sci. Appl.* **9**, 38 (2020).
- [30] B. Xie, H. Liu, H. Cheng, Z. Liu, J. Tian, and S. Chen, Dirac points and the transition towards Weyl points in three-dimensional sonic crystals, *Light Sci. Appl.* **9**, 201 (2020).
- [31] H. Qiu, M. Xiao, F. Zhang, and C. Qiu, Higher-order Dirac sonic crystals, *Phys. Rev. Lett.* **127**, 146601 (2021).
- [32] L. Luo, H.-X. Wang, Z.-K. Lin, B. Jiang, Y. Wu, F. Li, and J.-H. Jiang, Observation of a phononic higher-order Weyl semimetal, *Nat. Mater.* **20**, 794 (2021).
- [33] Q. Wei, X. Zhang, W. Deng, J. Lu, X. Huang, M. Yan, G. Chen, Z. Liu, and S. Jia, Higher-order topological semimetal in acoustic crystals, *Nat. Mater.* **20**, 812 (2021).
- [34] W. Deng, J. Lu, F. Li, X. Huang, M. Yan, J. Ma, and Z. Liu, Nodal rings and drumhead surface states in phononic crystals, *Nat. Commun.* **10**, 1769 (2019).
- [35] X.-P. Li, B. Fu, D.-S. Ma, C. Cui, Z.-M. Yu, and Y. Yao, Double Dirac nodal line semimetal with a torus surface state, *Phys. Rev. B* **103**, L161109 (2021).
- [36] Z.-M. Yu, Z. Zhang, G.-B. Liu, W. Wu, X.-P. Li, R.-W. Zhang, S. A. Yang, and Y. Yao, Encyclopedia of emergent particles in three-dimensional crystals, *Sci. Bull.* **67**, 375 (2022).
- [37] See the Supplemental Material at <http://link.aps.org/supplemental/10.1103/PhysRevApplied.20.064047> for the band dispersion of torus surface state, experimentally measured pressure distributions, impact of defects on topological surface state propagation, and surface spectra under open boundary conditions.
- [38] H. Qiu, Q. Zhang, T. Liu, X. Fan, and C. Qiu, Observation of fourfold nodal hinges and toruslike surface modes in acoustic metamaterials, *Phys. Rev. B* **108**, L201102 (2023).